A 2D and 3D segmentation-based microstructure study on the role of brittle phases in diffusion brazed AISI 304L/NiCrSiFeMoB joints

Johannes L. Otto [*], Lukas M. Sauer, Malte Brink, Thorge Schaum, Lars A. Lingnau, Marina Macias Barrientos, Frank Walther

TU Dortmund University, Chair of Materials Test Engineering, Dortmund 44227, Germany

ARTICLE INFO

ABSTRACT

Nickel-based filler metals are frequently used in high temperature vacuum diffusion brazing for austenitic stainless-steel joints when components are subjected to high static or dynamic loads, corrosive environments and elevated temperatures. Due to melting point depressing metalloids such as silicon and boron, hard and brittle intermetallic phases are formed during the brazing process depending on the diffusion mechanisms. These brittle phases significantly affect mechanical and corrosive properties of the compounds. To quantify the influences of their amount, morphology and distribution, deep learning image segmentation was applied to segment these phases of the athermal solidification zone and the diffusion zone. Subsequently, characteristic microstructure parameters were calculated from these. The parameters of six different brazed joint variations were compared with their experimental characterization of mechanical and corrosive properties so that several correlations could be identified. Finally, a layer-by-layer removal of a brazed joint was performed using a focused ion beam, and a 3D model was reconstructed from the generated images to gain a mechanism-based understanding beyond the previous 2D investigations.

1. Introduction

Diffusion brazing, also known as transient liquid phase (TLP) bonding [1,2], under vacuum atmosphere is an established process that is particularly suitable for joining highly stressed structures with multiple joints and assemblies that need to be joined with low distortion. The high degree of design freedom allows the joining from ultrathin-walled honeycomb structures to the full-surface joining of injection molds [3,4]. Brazing filler metals exist in numerous alloy systems, of which Au-, Pd–, Fe- or Ni-based alloys can be used for high temperature applications, since none of it has a solidus temperature below 800 °C and so their properties are stable at elevated temperatures [5]. Compared to the other base alloys, Ni-based filler metals offer several advantages for brazing austenitic stainless steels, such as moderate brazing temperatures, comparatively low material costs, good flow and wetting properties during brazing, and corrosive- mechanical capability properties that are comparable to the base material. Various elements can be used to lower the melting point of the filler, but the diffusible metalloids B, P and Si are particularly effective. Cr can also reduce the melting point, but its main function is to increase strength, heat and corrosion

resistance [6].

The NiCrSiB-system investigated in this study can therefore be suitable for numerous industrial applications. But a limiting factor, as for all Ni–based filler metals, are the intermetallic brittle phase formations like borides and silicides. The particularly light and small metalloid B can diffuse deeply into the base material along the austenite grain boundaries and forms a chemical bond with Cr and Fe of the base material even at low concentrations, so that in dependence on the brazing temperature typically $(Fe, Cr)_5B_3$ and $(Fe, Cr)_2B$ brittle phases are precipitated at the grain boundaries [7]. These phases can be used to mark the diffusion zone (DZ) [8] or as called diffusion affected zone (DAZ) [9] within the brazed joint, as shown in Fig. 1. In the following they will shortly be called DZ-phases. Their dissolution at high temperatures and very long holding times can be possible but is problematic for mechanical properties due to high grain growth [10]. In the center of the brazed joint other brittle phase formations can be found. With sufficient diffusion through a brazing temperature above the liquidus of the filler metal, long holding times and a small brazing gap width, a complete isothermal solidification of the melt starts, in which the solidus temperature is raised to the brazing temperature by diffusion of melting point

* Corresponding author.
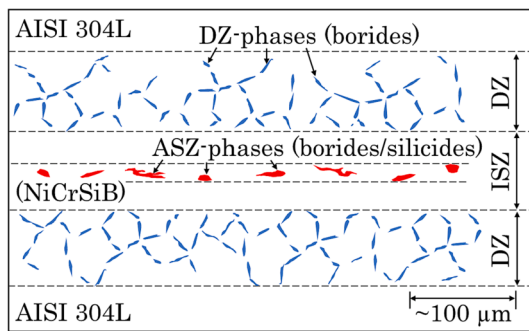 *E-mail address:* johannes.otto@tu-dortmund.de (J.L. Otto).

Fig. 1. Schematic drawing of the different zones and phases of a brazed AISI 304L/NiCrSiB joint.

depressant elements such as B. This area is therefore called in the following isothermal solidification zone (ISZ) and is free of brittle phases. With complete isothermal solidification, an improvement of the mechanical properties was observed in numerous studies [11–14]. If holding time or brazing temperature are not sufficient or the brazing gap width was too high, the remaining liquid enriches with melting point depressants like Si and B and a solidification can only start during cooling. Due to the enrichment of the melting point depressant metalloids, more eutectic phases such as borides and silicides will form in this area and mark the therefore named athermal solidification zone (ASZ), also known as non-isothermal solidification zone (NSZ) [15]. In the following, these brittle eutectic phases will just be called ASZ–phases. The structure and chemical composition of these phases varies more than that of the DZ-phases. ASZ-phases like CrB, Ni_3B and Ni_3Si have been identified in other studies [16–18]. Because ASZ-phases were separated from each other or absent at all in this study, the ASZ-zone itself will not be further analyzed and discussed, just the ASZ-phases.

Various approaches have been tested to reduce or separate these brittle phases to improve the mechanical and corrosive properties of the brazed joints and thus of the brazed components. These include adjustments to the brazing process parameters or alloy variations, such as the addition of titanium [19]. Also, mechanical approaches such as the use of foam structures for brittle phase separation were tested [20]. However, the aim of this study is to quantify the formation, spatial distribution and the effects of brittle phases to improve the understanding of the process-alloy-structure property relationships regarding the role of brittle DZ- and ASZ-phases.

2. Materials and experimental procedures

2.1. Materials

Three different experimental amorphous NiCrSiB filler metal foils with a thickness of 45 ± 5 μm were produced by rapid solidification on a rotating copper disk. The weight percent of Si and B was kept constant at 7.5 and 1.5 wt.-%, respectively. The Cr and Mo content and consequently also the Ni content were changed as shown in Table 1. An increase in Cr and Mo made the foils more brittle. The melting range was determined by applying differential scanning calorimetry (DSC) with a heating rate of 10 K/min up to 1300 °C. The determined solidus temperature T_S and liquidus temperature T_L are given in Table 1, too. With an increase in Cr

and Mo, T_L increases, which must be considered to interpret the results, regarding diffusion processes. Especially for the variant with 7 % Cr without molybdenum, which showed a significantly lower melting range. The base material used was the stainless metastable austenite AISI 304L (X2CrNi18-9, 1.4307), in the form of cold-drawn bar material of 16 mm diameter with a grain size before brazing of about 60 μm. The filler metal foils were placed in between two bars with grinded contact surfaces and a small fixation load of 500 g was applied, so that brazing of cylindrical butt joints with a constant gap size could be ensured. The brazing process time–temperature curves are given in Fig. 2. The heating was carried out in a first step with 20 K/min until 900 °C, which was below all determined filler metal solidus temperatures, and hold for 15 min to achieve a homogeneous heat distribution. In a second step the brazing temperature of 1160 °C was reached with 40 K/min and hold for 15 min in the first process mode or hold for 40 min in the second process mode.

Since two different holding times and three different filler metals were used, six different types of microstructures could be brazed, that are shown in Fig. 3 by means of scanning electron microscopy (SEM) images using the backscattered electron (BSE) detector. Boride phases appear darker and are present in the DZ and ASZ, while silicides appear lighter, especially when they are molybdenum enriched, and are present only in the ASZ. For the filler metal with 7 % Cr without Mo, no ASZ-phase formation was observed for both holding time modes, which means that the isothermal solidification must have already been completed after a short holding time. This is most likely due to the low melting range of this filler metal. An energy–dispersive X-Ray spectroscopy (EDX) analysis mapping of the variant 7 % Cr, 0 % Mo and 40 min, given in Fig. 3, shows a homogeneous element distribution inside the ISZ, and Cr-rich borides can be seen in the DZ, which are most likely $(Fe, Cr)_2B$ phases, according to EDX and [7]. In general, the longer holding times resulted in better diffusion, which increased the lengths of the different zones and affected the shape, number, size, and distribution of all brittle phases. This will be investigated in Chapter 3.2.
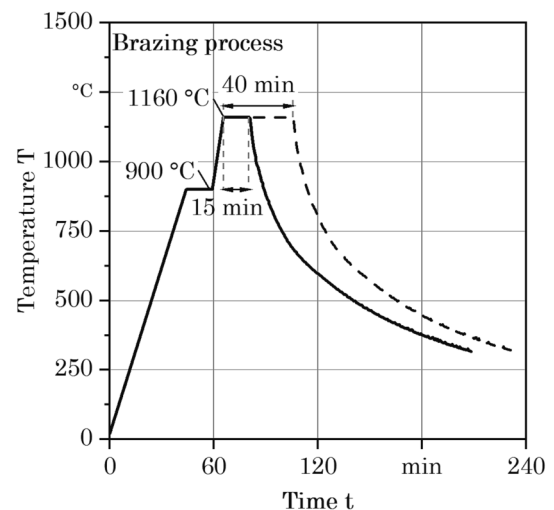

Fig. 2. Time-temperature curves of the brazing process with 15 and 40 min holding time.

Table 1
Chemical compositions and melting ranges of the base material and the filler metals.

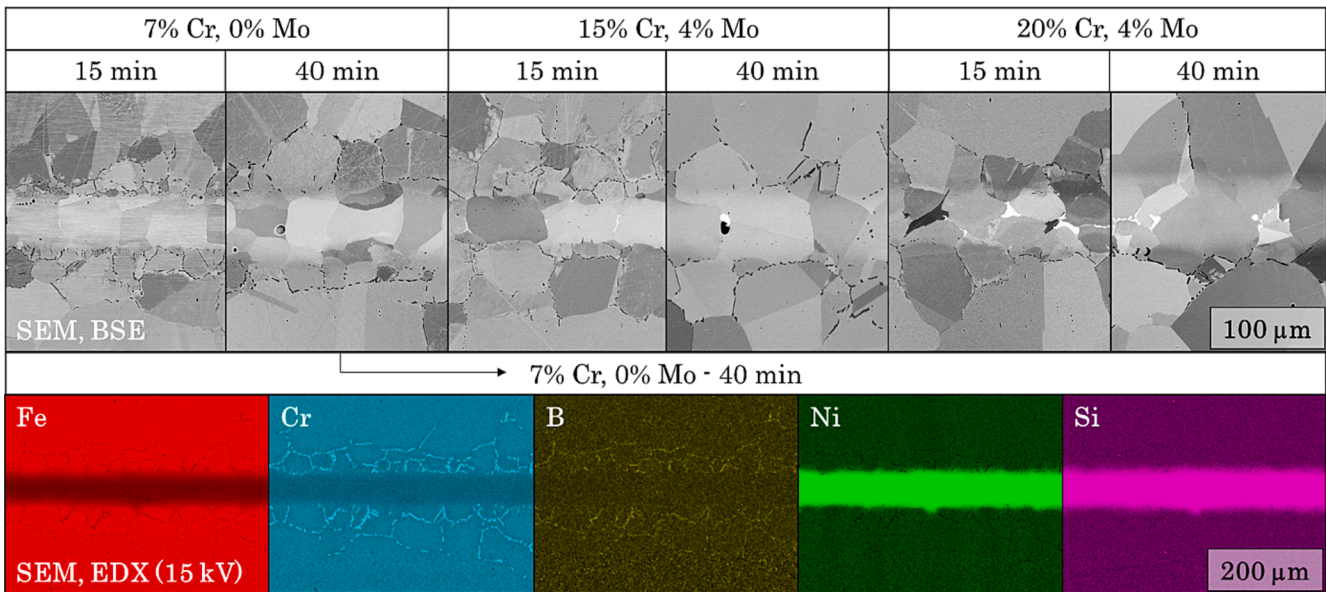| Alloy / name	T_S [°C]	T_L [°C]	Alloying elements, wt.-% max.									
			C	Cr	Ni	Mn	Si	P	S	Fe	Mo	B
AISI 304L	~ 1400	~ 1450	0.023	18.14	8.03	1.54	0.3	0.045	0.03	bal.	0.34	–
7 % Cr, 0 % Mo	966	1070	–	**7**	bal.	–	7.5	–	–	4	**–**	1.5
15 % Cr, 4 % Mo	1058	1123	–	**15**	bal.	–	7.5	–	–	4	4	1.5
20 % Cr, 4 % Mo	1079	1137	–	**20**	bal.	–	7.5	–	–	4	4	1.5

Fig. 3. Overview of the six microstructures of the brazed joints due to filler metal compositions and holding time variations based on SEM-BSE images and an EDX mapping of the 7 % Cr, 0 % Mo and 40 min variant.

2.2. Segmentation-based procedures

The following sections describe the methods used for the image acquisition, image segmentation, quantitative 2D microstructure analysis and 3D model generation, which are the focus of this study.

Image acquisition

For the quantitative 2D microstructure analysis, at least three images per variant were taken at different locations of the metallographic cross sections of each variant at a magnification of 500 × using a BSE detector on the SEM (resolution: 2048 × 1776 pixels). Sections of some of these images have already been shown in Fig. 3. For metallographic preparation, the cylindrical brazed specimens were first cut in half and conductively hot mounted to grind the cross sections down from P320 to P2500 using SiC abrasive papers. Diamond suspensions of 6, 3, and 1 μm were used for polishing, and the final surface was finished with an oxide polishing suspension.

For the time-consuming 3D model generation, only the variant of 7 % Cr, 0 % Mo and 40 min holding time was investigated. For this purpose, a cuboid was cut out in the center of the cylindrical brazed specimen and the surfaces were polished as described above. The further preparation took place within the FIB-SEM. Thin slices were ablated automatically by a focused ion beam (FIB) and high-resolution images were acquired every 20 nm using Inlens and SE detectors (resolution: 6720 × 6720 pixels). In order to be able to scan the entire brazed joint width, a large [21] slice width of almost 140 μm was set, which led to the increased formation of artifacts, which subsequently had to be removed via deep learning image segmentation. Improving the resolution would also be possible [22], but has not been done.

Segmentation

For the image segmentation the software Zeiss Zen Analyzer with its module Zen Intellesis was used. Based on deep learning algorithm [23] a training of models for the segmentation of different phases and different SEM-BSE images was carried out to identify and segmentate the brittle phases automatically and reliable, as shown in Fig. 4. Using the integrated analysis functions of Zen Analyzer several useful information like number, area, coordinates or geometric sizes (e.g. diameter or elliptic semi axis) could be extracted directly without a self-programmed algorithm.

Microstructure parameter calculation
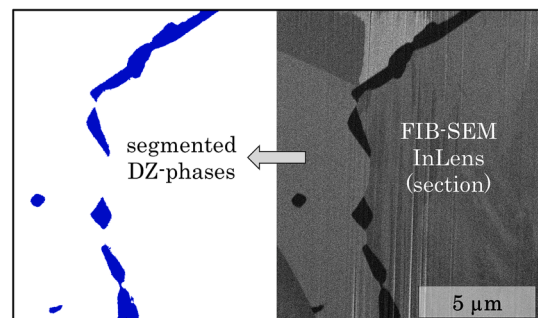
The obtained data were then further processed using self-

Fig. 4. Example of segmented DZ-phases.

programmed python-based algorithms. First, the size of the analysis area was reduced to 400 × 400 μm (1776 × 1776 pixels) and the segmented objects were centered as much as possible. Then small objects below 10 pixels were filtered out, which can be considered as mis-segmentations. Afterwards, a tilt angle correction was performed to always align the ISZ as horizontally as possible. Then the accumulated area of DZ- and ASZ-phases were calculated form numbers and area of the individual phases. The mean circumference was approximated by considering the DZ-phases as ellipses and was calculated based on the elliptical semiaxes. Subsequently, for the DZ-phases, 5 % of the segmented objects above and below the DZ were filtered out to reduce outliers and make the characteristic values more robust. Then the ISZ- and the DZ-length could be determined as shown in Fig. 5. As mentioned above, the length of the ASZ was not considered. If there was an ASZ in a variant, it was included in the length of the ISZ to reduce the complexity of subsequent analyses.

Correlation analysis and statistics

The microstructure parameters generated were used to analyze them for correlations to the experimentally determined mechanical and corrosive results. The sample Pearson correlation coefficient for linear correlation $r_{xy,linear}$ was calculated as given in (1) where n is the sample size, x_i and y_i are the individual sample points and x^- and y^- are the sample mean. To investigate also simple exponential and quadratic correlations a transformation of the y–values was carried out (2). The coefficient of determination r^2 was calculated from r_{xy} (3) and therefore does not refer to a higher mathematical function, which of course can fit
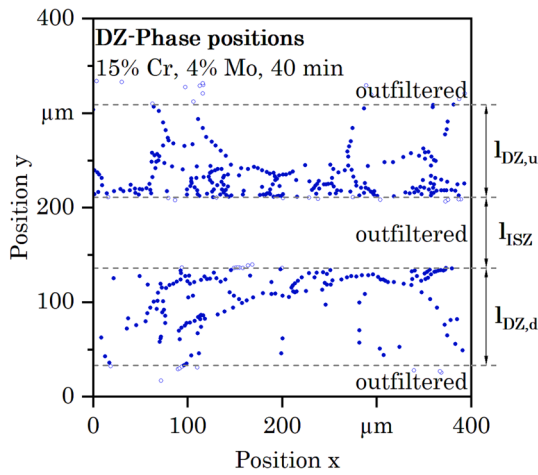
Fig. 5. Calculation of ISZ- and DZ-length based on segmented DZ-phases.

better and achieve higher r^2 values but would distort the result for only six variant types.

$$r_{xy,linear} = \frac{\sum_{i=1}^{n}(x_i - \bar{x}) \times (y_i - \bar{y})}{\sqrt{\sum_{i=1}^{n}(x_i - \bar{x})^2 \times \sum_{i=1}^{n}(y_i - \bar{y})^2}} \quad (1)$$

$$r_{xy,exponential} \rightarrow y = \log(y)$$
$$r_{xy,quadratic} \rightarrow y = \sqrt{(y)} \quad (2)$$

$$r^2 = (r_{xy})^2 \quad (3)$$

For all error bar plots in this study, the standard error of the sample mean was calculated, which is of more interest than the absolute range or standard deviation.

3D model generation

Fig. 6 shows an example of the first steps in the processing of the FIB-SEM-Inlens images. From 1243 images, an area with low artifacts density was cut out to create a 3D model of 139.5 × 19.5 × 24.9 µm (5502 × 768 pixels each image). The automated cutting of the images was done in the opensource software FIJI (ImageJ). For better processing, the images were again divided into over 5000 individual images. Using Zen Intellesis, the brittle phases were now segmented from the image stacks. Using FIJI, the pixels were then processed into voxels, and several small models were generated as mesh structures into .obj–format. To create a
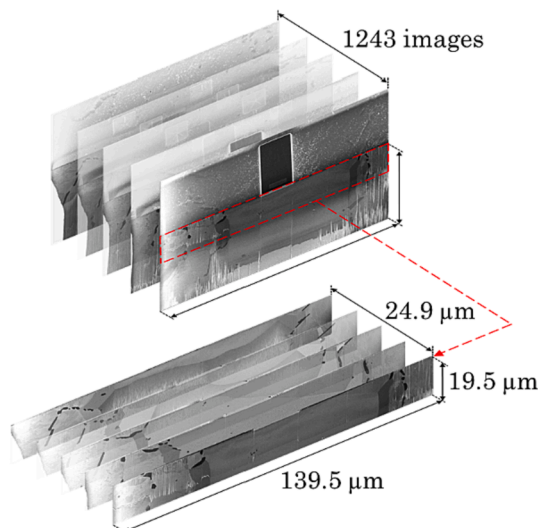

Fig. 6. Processing of the FIB-SEM-Inlens images.

solid model from the mesh structures, a mesh-enabler was used and then all the individual parts were combined into an assembly - the final model - using the computer aided design (CAD) software Autodesk Inventor. For a better representation, the model was then rendered.

2.3. Experimental procedures

The following is a brief description of the mechanical, corrosive, and corrosive-mechanical tests that were used to explain failure mechanisms and for the correlation analyses in Chapter 3.3. Detailed descriptions of the experiments performed can be taken from [24,25,26]. Corrosion tests were performed following the Strauss test for the investigation of intergranular corrosion resistance, according to EN ISO 3651–2 with some modifications. The specimens were boiled for 8 h at 110 °C in sulfuric acid (250 ml/L H_2SO_4) with copper sulfate (50 g/L $CuSO_4$) and copper chips (100 g/L Cu). The specimens were then cut to measure the depth of corrosion from the surface into the material [25]. The pendulum impact tests were performed with an impact energy of 150 J and a specimen geometry according to ISO 148–1 of 10 × 10 × 55 mm, but no notch was added because the brazing seam in the center of the specimen already served as a stress concentrator. For the tensile and fatigue tests, the cylindrical butt joints were turned to a test geometry according to ISO 6892–1 with a test diameter of 8 mm and then polished. Tensile tests were performed according to ISO 6892–1 with low strain rate (0.00025 s-1) [26]. The load increasing multiple amplitude fatigue tests (MAT) were carried out inside a self-developed corrosion chamber that was constantly flown through by the moderate corrosive synthetic exhaust gas condensate K2.2 according to VDA 230–214 [24,27]. The following test parameters describe the mechanical load during the MAT: frequency f = 10 Hz, load ratio R = 0.1 (tension–tension), step length $\Delta N = 10^4$ load cycles and step height $\Delta\sigma_{max}$ = 5 MPa. The maximum stress reached at failure $\sigma_{max,f}$ was used as parameter for the correlation analysis.

3. Results and discussions

3.1. Corrosive and mechanical failure mechanism

To gain an understanding of the critical effects of the brittle phases in the brazed joint, which is necessary for the interpretation of the following results, the following describes the identified mechanical and corrosive failure mechanisms for the investigated variants.

Fig. 7 a) shows a fatigue crack of the variation with 7 % Cr without Mo and 40 min holding time at the end of a MAT that reached a maximum stress until failure $\sigma_{max,f}$ = 380 MPa, before the test was stopped due to specimen failure. The crack stage can be described as an early forced fracture area. It was found that the Cr-rich borides in the DZ break before the crack reaches them. Fig. 7 b) shows from microhardness indentations that the Cr-rich borides have an extremely low plastic deformation capacity compared to the surrounding material. This is also visible from the topography images of the indentations using atomic force microscopy (AFM). Interestingly, due to the metallographic preparation, a deepening can be detected at the phase boundary between the austenitic base material and the Cr-rich borides. It presumably corresponds to the local chromium depletion zone and thus a local hardness reduction. However, especially in the force fracture region, a strong deformation occurs which exceeds the elastic and plastic deformation capacity of the Cr-rich borides and thus leads to fracture within the surrounding material. Micropores form at the fracture sites, which can presumably grow into larger pores at sites of high deformation and start their own crack initiation. This can explain that in the region of the force fracture, jumping of the crack from one DZ to the other has been observed for complete isothermal solidification [27]. In the case of strong ASZ-phase formation, this dominates the fracture progression and a brittle crack development occurs along the ASZ-phases [24]. This is mainly because these are distributed in a chain-like formation in the
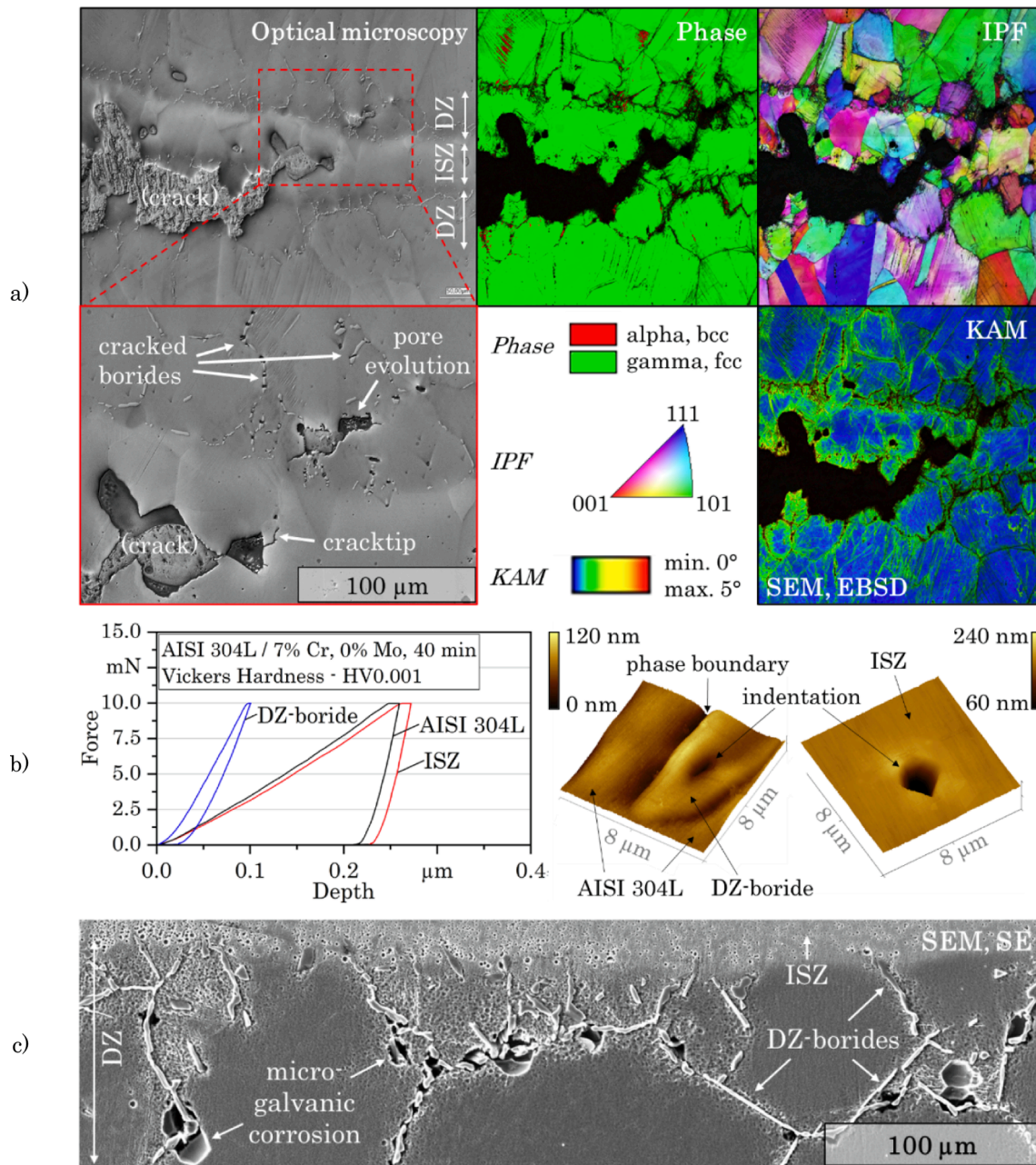
Fig. 7. Variation with 7 % Cr, 0 % Mo and 40 min holding time a) mechanism of fatigue crack propagation in a load increase test by means of optical microscopy and SEM-EBSD, b) instrumented microhardness investigations and indentation analysis with AFM and c) micro galvanic corrosion at Cr–rich borides in diffusion zone by electro polishing (10 V, 10 s) in oxalic acid.

center of the brazed seam and are thus located in the area of the highest deformation. The significant deformation can also be recognized by EBSD using the kernel average misorientation (KAM) mapping. Deformation-induced martensite formation (alpha, bcc) of the meta-stable austenite can be seen in the phase mapping and was found only to a small amount and does not appear to affect crack propagation as much as the brittle phases. But in the case of corrosion fatigue, an increased tendency to stress corrosion cracking due to martensite formation should be considered [28–30]. An inter-transcrystalline mixed fracture can be observed by inverse pole figure (IPF) mapping, with the trans-crystalline part being located more in the ISZ, while the small grain structure at the transition to the DZ and the Cr–rich boride formation on the grain boundaries support the intercrystalline part.

Fig. 7 c) shows an example of the micro galvanic corrosion mecha-nisms occurring in the DZ caused by local differences in the

electrochemical potential of Cr–rich borides to the chromium-depleted surrounding base material. While the Cr-rich borides act as a cathode, the surrounding chromium depleted zone acts as an anode and dissolves. The surrounding matrix around this zone, which is not depleted of Cr, must be considered as another important cathode as shown for Cr–rich carbides in [31]. This effect was also observed at the ASZ-phases, but the highest corrosion attack for all investigated variants in this study was observed in the DZ.

3.2. Segmentation and quantification

Fig. 8 shows 3D plots of the size distributions of the individual brittle phases in terms of their mean area versus their position in the X and Y directions on an area of 300 × 300 μm from a single exemplary segmented image out of each variant. It shows that ASZ-phases generally
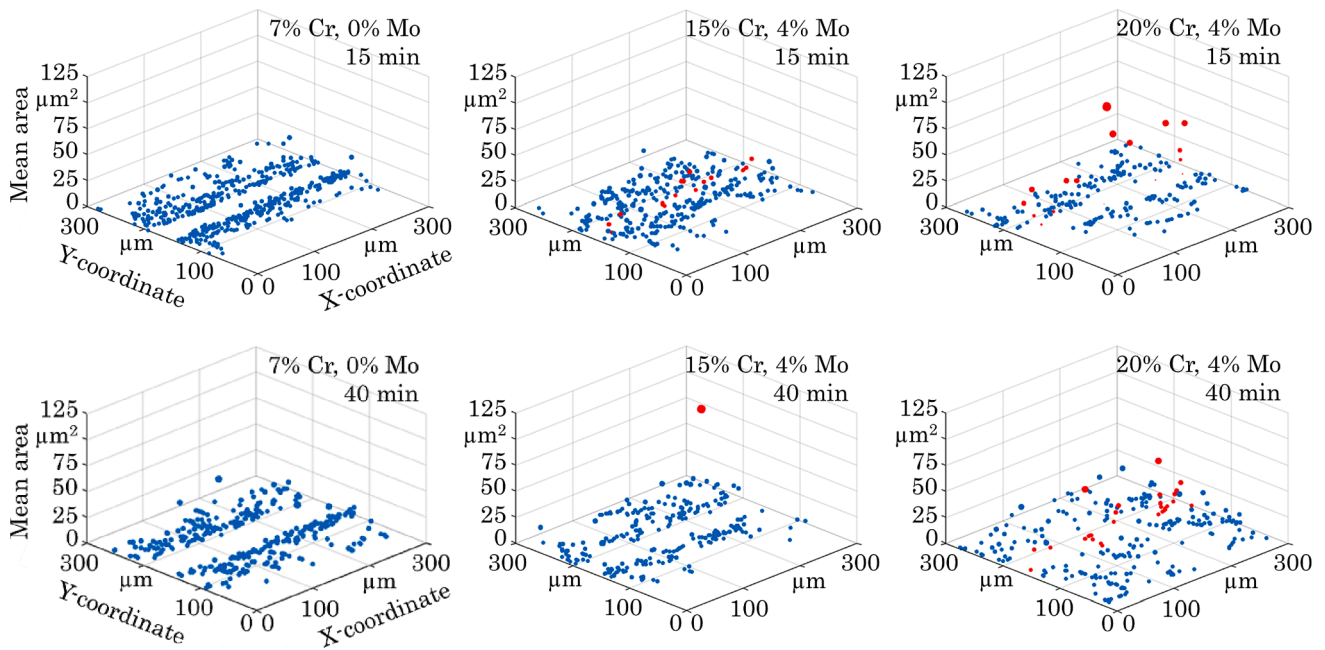
Fig. 8. Distribution and mean area of DZ-phases (blue) and ASZ-phases (red) for all studied variants from one exemplary segmented image per variant (shown segmentation area per variant: 300 × 300 μm). (For interpretation of the references to colour in this figure legend, the reader is referred to the web version of this article.)

have a larger mean area than DZ-phases. As mentioned in Chapter 2.1, no ASZ-phases could be found in the 7 % Cr variants without Mo. Instead, significantly more and smaller DZ-phases can be seen in this variant. The variant with 20 % Cr and 4 % Mo contained the most ASZ-phases. It can already be seen from Fig. 8 that the ISZ- and DZ-length increase with longer holding times. In addition, the phases tend to

agglomerate with longer holding times as the number of phases decreases and sizes tend to increase.

Calculated microstructure parameters, such as the lengths of the DZ- and ISZ–zones, the number of DZ- and ASZ–phases, and the accumulated areas of the DZ- and ASZ-phases are given in Fig. 9. The calculated parameters are based on the evaluation of at least three randomly selected
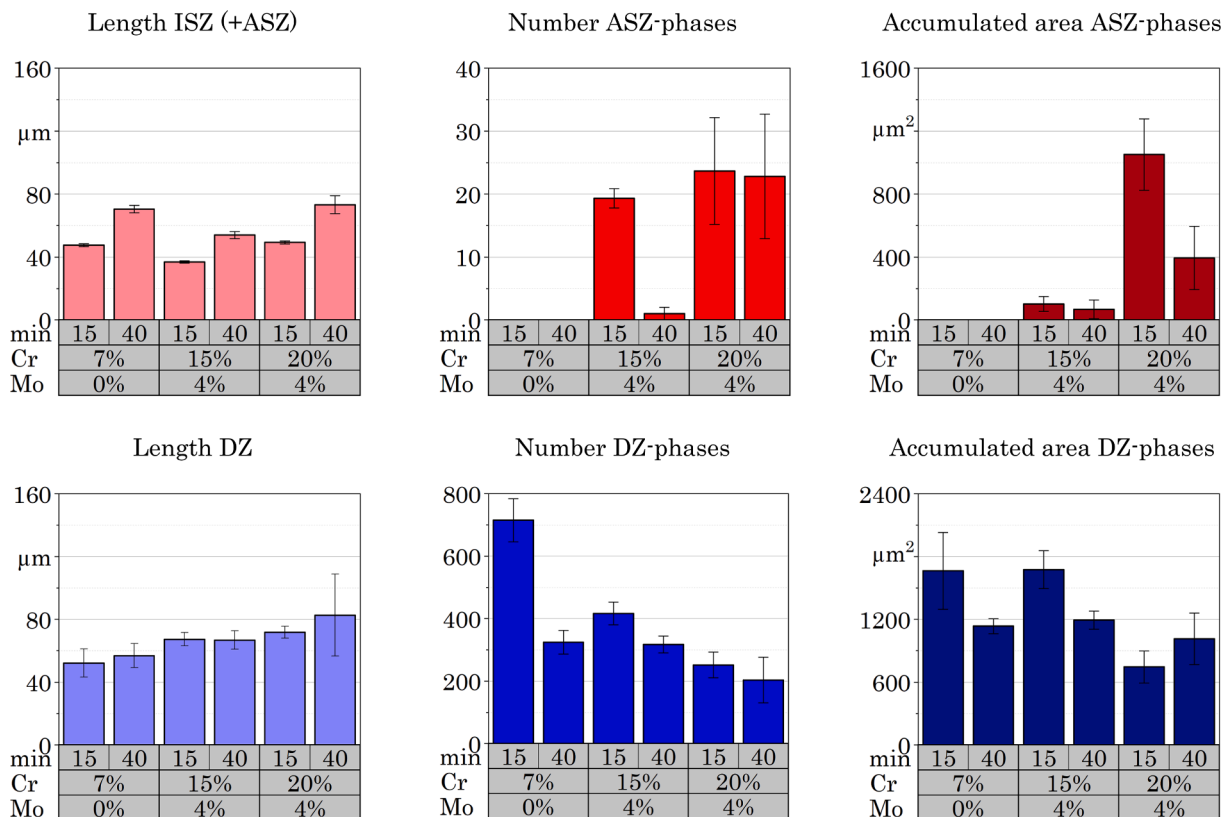
Fig. 9. Calculated parameters from the segmented DZ- and ASZ-phases (segmentation area: 400 × 400 μm).

400 × 400 μm areas along the brazed joint per variant. Due to the significantly lower number of ASZ-phases, parameters based on these phases show a significantly higher standard error of the sample mean. The accumulated area of the phases must be taken into account when considering the number of phases, as can be seen in Fig. 8, higher holding times result in larger phases with a simultaneous reduction in the number. The length of the DZ shows a high dependence on the alloy and thus on the chemical potential between filler metal and base material. So, the two higher alloyed filler metal variants that containing 4 % Mo show higher diffusion depths. Compared with the length of the ISZ (and ASZ), the DZ–length shows a lower dependence on the holding time. The general growth of the DZ and ISZ due to holding time was observed in different studies [32,33].

3.3. Correlation analysis

To evaluate the significance of the microstructure parameters determined in Chapter 3.2 regarding the failure mechanisms, these were analyzed for correlations with results from corrosive, mechanical and corrosive-mechanical experiments (briefly described in Chapter 2.3) for all six microstructure variants.

According to the equations (1) to (3), the r^2-values for simple linear, exponential and quadratic relationships between the experimental results and the calculated microstructure parameters were determined and summarized as a matrix in Table 2. Some selected correlations are plotted in Fig. 10. It should be noted that these correlations do not necessarily have to describe the material causes of the properties directly, but at least they can be considered as indicators. For example, some of the parameters show correlations with each other or depend on factors such as chemical potential and grain size, which influence the properties themselves.

No correlation at all could be found for the length of the ISZ (+ASZ). For the length of the DZ a moderate correlation was found with the corrosive and corrosion fatigue results. Therefore, determining the length of the zones proves not that suitable for making statements about the properties of the brazed joint. The number of phases, on the other hand, shows to be a more suitable parameter. With a higher number of ASZ–phases, a reduction of the maximum stress of the MAT corrosion fatigue tests was observed, caused by crack propagation along these phases. With a higher number of DZ-phases, a decrease in corrosion resistance was observed. Since the accumulated area of the DZ-phases does not correlate with the corrosion properties, many small DZ–phases seem to promote corrosion. This leads to the conclusion, that an absolute chromium depletion (in wt.-%) within the DZ due to the formation of the Cr-rich borides does not seem to be a determining factor, but instead the interfaces of the micro-galvanic elements and the surrounding chromium-depleted zone. For this reason, the average circumference of the DZ–phases, approximated by a consideration of the phases as ideal ellipses, was considered. This appears to be more suitable for providing information about the corrosive properties. For the mechanical properties, the accumulated area of the ASZ-phases proves to be the most influencing microstructure parameter allowing statements within this study. This is consistent with the finding from several studies that have identified a high importance of ASZ–phases for mechanical properties [34,35].

3.4. 3D morphology reconstruction

Fig. 11 shows in two perspectives the rendered 3D CAD model of DZ-phases, ASZ-phases and a few pores segmented and generated from 1243 single images of the ASZ-phase-free brazed seam variant with 7 % Cr, 0 % Mo and 40 min holding time. The background shows the last Inlens image of the FIB scan (with some artifacts in the investigated area and the markers on the top of the specimen) to get a 3D impression of the position of the model. It provides valuable new insights to interpret the previous 2D results.

The results show that there are hardly any isolated DZ–phases, but instead a strongly interconnected structure is present. This interconnected structure consists of plate-like shapes, which are oriented along the grain boundaries. The morphology of the Cr–rich borides separates the surrounding austenite grains (matrix) and thus provides strong microstructural notch effects. The deformation limited by the brittle phases cannot be compensated by deformation of the matrix and thus leads to the fractures of the borides inside the matrix as shown in Fig. 7a), which under further deformation led to a pore evolution and accelerated crack propagation. The morphology also leads to a high specific interface and thus a high surface energy, which influences corrosion, demonstrated in the previous correlation analyses and Fig. 7c). It is also important to consider the surrounding chromium-depleted zone around the Cr–rich borides. This also affects the influence of the microstructural notch effects via a local hardness and strength reduction, as indirectly shown by Fig. 7b).

Table 2
R^2-matrix for identification of linear, exponential and quadratic microstructure-property correlations (calculated according to equations 1–3).

	Corrosion depth [μm]			Tensile strength [MPa]			Impact toughness [J/cm^2]			Maximum stress MAT [MPa]		
	Corrosive			Quasistatic			Impact			Corrosion fatigue		
Length ISZ (+ASZ) [μm]	L:0.03	E:0.00	Q:0.01	L:0.06	E:0.05	Q:0.06	L:0.18	E:0.10	Q:0.15	L:0.02	E:0.02	Q:0.02
Length DZ [μm]	L:0.56	E:0.45	Q:0.58	L:0.27	E:0.20	Q:0.23	L:0.20	E:0.14	Q:0.18	L:0.64	E:0.59	Q:0.62
Number ASZ-phases [-]	L:0.28	E:0.10	Q:0.24	L:0.54	E:0.46	Q:0.50	L:0.70	E:0.50	Q:0.65	L:0.86	E:0.83	Q:0.84
Number DZ-phases [-]	L:0.77	E:0.38	Q:0.62	L:0.22	E:0.19	Q:0.20	L:0.01	E:0.04	Q:0.04	L:0.35	E:0.34	Q:0.34
Circumference DZ-phases [μm]	L:0.73	E:0.67	Q:0.78	L:0.00	E:0.00	Q:0.00	L:0.00	E:0.02	Q:0.00	L:0.15	E:0.11	Q:0.13
Accumulated area ASZ-phases [μm^2]	L:0.09	E:0.00	Q:0.04	L:0.95	E:0.95	Q:0.96	L:0.60	E:0.91	Q:0.80	L:0.82	E:0.85	Q:0.85
Accumulated area DZ-phases [μm^2]	L:0.22	E:0.03	Q:0.12	L:0.43	E:0.44	Q:0.44	L:0.05	E:0.29	Q:0.15	L:0.35	E:0.37	Q:0.37

L: linear, E: exponential, Q: quadratic (the greener, the higher the correlation).
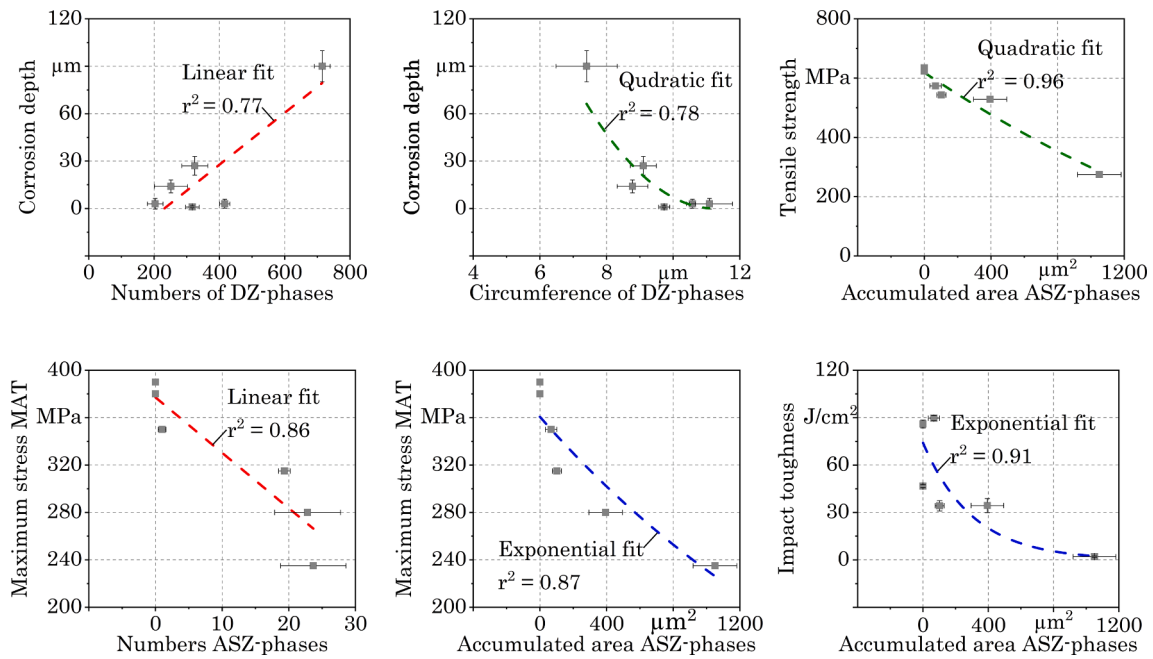
Fig. 10. Exemplary microstructure-property correlations, selected from Table 2, for corrosive and mechanical experimental results and the DZ-/ASZ-phases-based microstructure parameters.
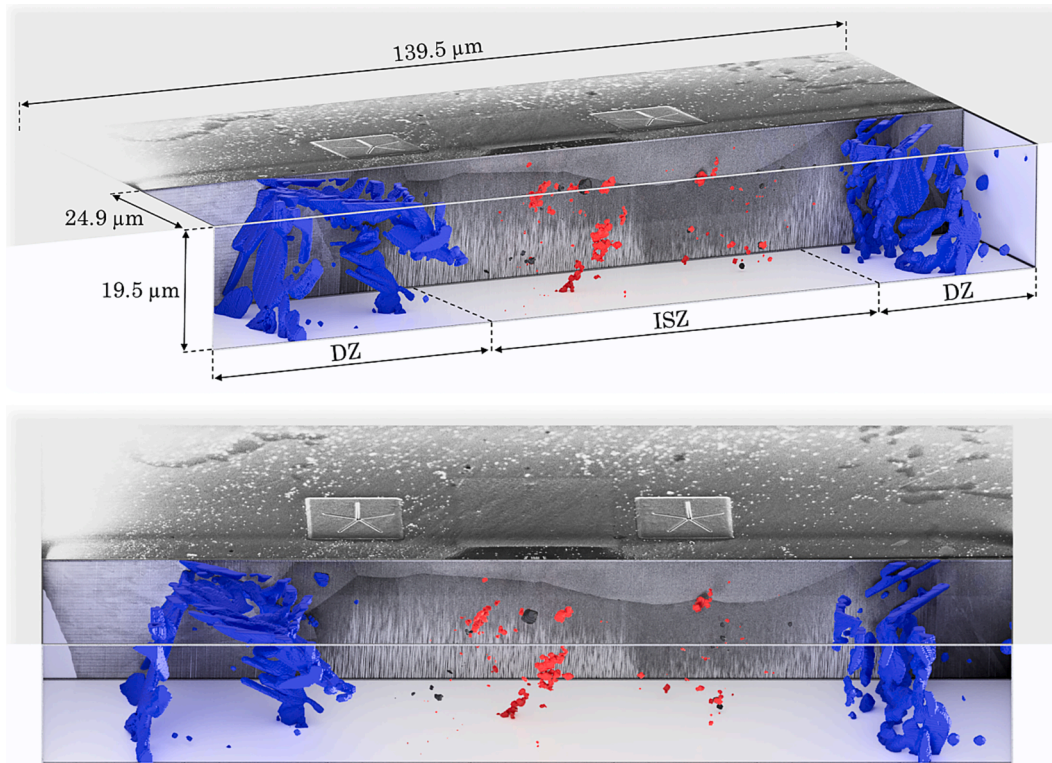

Fig. 11. Rendered 3D CAD model in two perspectives of the DZ-phases structure (blue), which consist mainly of Cr–rich borides at the austenite grain boundaries, as well as small ASZ-phases (red) consisting mainly of Ni-rich borides and a few pores (black) inside the ISZ of the variant 7 % Cr, 0 % Mo and 40 min holding time (brazing temperature 1160 °C). (For interpretation of the references to colour in this figure legend, the reader is referred to the web version of this article.)

The assumption in Chapter 3.2 and Chapter 3.3, that in 2D–cross sections isolated Cr-rich borides are present must therefore be revised and it seems impossible to quantify the actual number of phases from a cross section. Two single appearing phases can be grown together to a single phase already 5 μm deeper. Therefore, instead of "number of DZ–phases", it should correctly be called "number of DZ-phases piercing points" at the surface of the cross section. For the same reason, it is not practical to determine the distance between single DZ-phases from 2D cross sections. However, the lengths of the zones can be well estimated. The ISZ-length of about 70 μm corresponds well to the ISZ-length calculated from 2D data for this variant. The 3D analysis offers the possibility to calculate further characteristic parameters with focus on

morphology. For example, volume- or interface-based parameters. The volume of the DZ-phases in the investigated area of Fig. 11 is 1359 μm^3, which corresponds to a volume fraction of almost 2 % of the whole segmented cuboid and within the DZ, the volume fraction of the DZ-phases corresponds to about 4.6 %.

Although this 7 % Cr, 0 % Mo, 40 min variant was considered to be free of ASZ–phases based on the previous studies, unconnected but partially agglomerated ASZ–phases with small diameters of about 0.2 to 2 μm were found, which are presumably Ni–rich borides. These ASZ-phases could not be detected based on 2D-SEM, as can be seen in Fig. 3 by BSE and EDX scans. The reason for this is assumed to be that these brittle phases break out of the ISZ during the preparation of the metallographic cross-sections due to their small size and isolation from each other. The volume fraction of these ASZ–phases in the ISZ is about 0.08 %, which is about a factor of 57 less than the volume fraction of the DZ–phases in the DZ. Nevertheless, only an almost complete isothermal solidification can be mentioned.

In addition, the pores within the ISZ were reconstructed in Fig. 11. Their origin can be attributed to gas inclusions or shrinking effects during solidification. Some pores seem to have formed directly at the ASZ-phases, which can be explained as a result of a higher volume reduction of the remaining eutectic melt during the athermal solidification compared to the surrounding ISZ, that has already solidified. This type of pore formation at the ASZ-phases probably occurs more strongly in the variants with larger ASZ-phases, which may indirectly increase the correlations between ASZ–phases and mechanical properties found in Chapter 3.3. For this variant, the volume fraction of the pores within the ISZ is comparatively low at about 0.02 %. Nevertheless, it must be assumed that these pores have an influence on crack propagation. The fatigue fracture progression presented in Fig. 7a) shows a "jumping" of the crack path from one DZ to the other DZ. These jumps are most likely promoted by these pores, since they will grow under serve deformation and form incipient cracks themselves, which then merge with the fatigue fracture.

4. Summarization and conclusions

The main mechanical and corrosive failure mechanisms of vacuum diffusion brazed AISI 304L/NiCrSiB were described in this study based on the role of different brittle phases. A novel concept for quantitative microstructure–property analysis of brazed joints was applied by first segmenting brittle phases using deep learning image segmentation. These were then used to calculate microstructure parameters, which were used for a correlation matrix with experimental results.

It was found that smaller and finer DZ-phase networks with a higher specific surface area reduce the corrosion resistance more than larger structures with the same accumulated area but a lower specific surface area. It may be assumed that this effect is also valid for ASZ–phases, which in this study were larger and more agglomerated than the DZ–phases and showed better corrosion resistance.

For the mechanical properties, high correlations could be identified with several parameters of the ASZ–phases, which dominate the crack propagation if they are present in case of an incomplete isothermal solidification.

Overall, the brittle phase-based microstructure parameters proved to be suitable for a comparative estimation of the mechanical and corrosive properties between different microstructure variants. For an accurate prediction of the properties, other influencing factors such as joint geometry effects, grain sizes, hardness gradients, pores and residual stresses must be considered for all variants, which was not part of this study. These are known to influence the capability properties as well as brittle phases.

For the first time, a large scale and high resolution 3D model could be created for the brittle phase structure of a AISI 304L/NiCrSiB brazed joint by the combination of FIB–SEM, deep learning image segmentation and CAD. The plate- and network-like morphology inside the DZ shows

that Cr-rich borides cannot be viewed isolated from 2D views. Even in brazed joints previously classified as ASZ-free, small ASZ–phases exist that remain unnoticed due to preparation without FIB. In addition, a low pore fraction could be detected, which is partly caused by the solidification of ASZ–phases. The model allows an interpretation of the morphological aspects on microstructural notch effects, crack propagation, the corrosion mechanisms, and thus the failure mechanisms of the brazed joints.

Using the finite element method (FEM), analyses are planned on the 3D model to further investigate the mechanical influences of the brittle phases and pores. For the corrosive properties, Kelvin probe force microscopy (KPFM) measurements are planned to improve the understanding of the effects of brittle phase formation on the surface potential and thus the local corrosion behavior.

Declaration of Competing Interest

The authors declare that they have no known competing financial interests or personal relationships that could have appeared to influence the work reported in this paper.

Data availability

All raw/processed data required to reproduce these findings are available from the authors upon reasonable requests.

References

[1] G.O. Cook III, C.D. Sorensen, Overview of transient liquid phase and partial transient liquid phase bonding, J. Mater. Sci. 46 (2011) 5305–5323, https://doi.org/10.1007/s10853-011-5561-1.

[2] D.H. Jung, A. Sharma, M. Mayer, J.P. Jung, A Review on Recent Advances in Transient Liquid Phase (TLP) Bonding for Thermoelectric Power Module, Rev. Adv. Mater. Sci. 53 (2) (2018) 147–160, https://doi.org/10.1515/rams-2018-0011.

[3] Y. Lou, X. Song, S. Hu, W. Fu, X. Chen, J. Cao, Evaluation of mechanical properties and vacuum brazing for TiAl/GH3536 hetero-honeycomb sandwich ultrathin-walled structure, Welding in the World 66 (2022) 1999–2015, https://doi.org/10.1007/s40194-022-01319-z.

[4] M. Boretius, The Potential of Vacuum Brazing-State of the Art and Developments from the Perspective of a Service Contractor, Adv. Eng. Mater. 8 (3) (2006) 158–161.

[5] M. Way, J. Willingham, R. Goodall, Brazing filler metals, Int. Mater. Rev. 65 (2020) 257–285, https://doi.org/10.1080/09506608.2019.1613311.

[6] M.A. Penyaz, A.A. Ivannikov, O.N. Sevryukov, B.A. Kalin, Overview of nickel-based filler metals for brazing of austenitic stainless steels, Non-Ferrous Met. (2021) 41–56, https://doi.org/10.17580/nfm.2021.01.06.

[7] H. Ma, P. Duan, P. Liao, G. Zhou, S. Tu, Effect of Temperature on Metallurgical Reactions and Microstructure Evolution of 316L/BNi-2 Brazed Joints, J. Mater. Eng. Perform. 31 (2022) 1631–1641, https://doi.org/10.1007/s11665-021-06296-w.

[8] L.X. Zhang, Z. Sun, Q. Xue, M. Lei, X.Y. Tian, Transient liquid phase bonding of IC10 single crystal with GH3039 superalloy using BNi2 interlayer: Microstructure

and mechanical properties, Mater. Des. 90 (2016) 949–957, https://doi.org/10.1016/j.matdes.2015.11.041.

[9] B. Binesh, Diffusion brazing in IN718/AISI 316L dissimilar joint: Microstructure evolution and mechanical properties, J. Manuf. Process. 57 (2020) 196–208, https://doi.org/10.1016/j.jmapro.2020.06.025.

[10] A. Ghasemi, M. Pouranvari, Thermal processing strategies enabling boride dissolution and gamma prime precipitation in dissimilar nickel-based superalloys transient liquid phase bond, Mater. Des. 182 (2019), 108008, https://doi.org/10.1016/j.matdes.2019.108008.

[11] A. Doroudi, A.E. Pilehrood, M. Mohebinia, A. Dastgheib, A. Rajabi, H. Omidvar, Effect of the isothermal solidification completion on the mechanical properties of Inconel 625 transient liquid phase bond by changing bonding temperature, J. Mater. Res. Technol. 9 (5) (2020) 10355–10365, https://doi.org/10.1016/j.jmrt.2020.07.015.

[12] H. Tazikeh, S.E. Mirsalehi, A. Shamsipur, Relationship of isothermal solidification completion and precipitate formation with mechanical properties of Inconel 939 joints vacuum TLP bonded by an amorphous Ni-Cr-Fe-Si-B filler alloy, J. Mater. Res. Technol. 18 (2022) 4762–4774, https://doi.org/10.1016/j.jmrt.2022.04.139.

[13] A.D. Jamaloei, A. Kohrram, A. Jafari, Characterization of microstructure and mechanical properties of dissimilar TLP bonding between IN718/IN600 with BNi-2 interlayer, J. Manufactur. Process. 29 (2017) 447–457, https://doi.org/10.1016/j.jmapro.2017.09.010.

[14] E. Norouzi, M. Atapour, M. Shamanian, A. Allafchian, Effect of bonding temperature on the microstructure and mechanical properties of Ti-6Al-4V to AISI 304 transient liquid phase bonded joint, Mater. Des. 99 (2016) 543–551, https://doi.org/10.1016/j.matdes.2016.03.101.

[15] Y. Zhang, Y. Cheng, N. He, C. Chen, Z. Gao, X. Gong, R. Wang, L. He, Microstructural characterization of TLP bonded joints of Mar-M247 superalloys with Ni-Cr-B interlayer, Mater Charact 198 (112766) (2023) 1–9, https://doi.org/10.1016/j.matchar.2023.112766.

[16] F. Arhami, S.E. Mirsalehi, A. Sadeghian, M.H. Johar, The joint properties of a high-chromium Ni based superalloy made by diffusion brazing: Microstructural evolution, corrosion resistance and mechanical behavior, J. Manuf. Process. 37 (2019) 203–211, https://doi.org/10.1016/j.jmapro.2018.11.025.

[17] J. Ruiz-Vargas, N. Siredey-Schwaller, N. Gey, P. Bocher, A. Hazotte, Microstructure development during isothermal brazing of Ni/BNi-2 couples, J. Mater. Process. Technol. 213 (2013) 20–29, https://doi.org/10.1016/j.jmatprotec.2012.07.016.

[18] B. Binesh, A. Jazayeri Gharehbagh, Transient Liquid Phase Bonding of IN738LC/MBF-15/IN738LC: Solidification Behavior and Mechanical Properties, J. Mater. Sci. Technol. 32 (11) (2016) 1137–1151, https://doi.org/10.1016/j.jmst.2016.07.017.

[19] K. Bobzin, H. Heinemann, M. Erck, S. Vinke, Influence of Ti inoculation on the wetting behaviour and microstructure of various Ni-based brazing alloys in combination with X5CrNi18-10, Weld. Cut. (2023) 16–22, https://doi.org/10.53192/WAC202301WAC16.

[20] B. Zhang, Q. Chang, Z. Sun, D. Li, H. Pan, L. Zhang, A concept of regulating the distribution of continuous brittle phases by spatial division of the Ti3SiC2/Ti2AlNb brazing seam, Mater. Des. 221 (2022) 110941–110951, https://doi.org/10.1016/j.matdes.2022.110941.

[21] C.S. Xu, K.J. Hayworth, Z. Lu, P. Grob, A.M. Hassan, J.G. García-Cerdán, K.K. Niyogi, E. Nogales, R.J. Weinberg, H.F. Hess, Enhanced FIB-SEM systems for large-volume 3D imaging, Enhanced FIB-SEM Systems for Large 6 (2017) e25916, https://doi.org/10.7554/eLife.25916.

[22] K. Hagita, T. Higuchi, H. Jinnai, Super-resolution for asymmetric resolution of FIB-SEM 3D imaging using AI with deep learning, Sci. Rep. 8 (1) (2018), https://doi.org/10.1038/s41598-018-24330-1.

[23] K. Choudhary, B. DeCost, C. Chen, A. Jain, F. Tavazza, R. Cohn, C.W. Park, A. Choudhary, A. Agrawal, S.J.L. Billinge, E. Holm, S.P. Ong, C. Wolverton, Recent advances and applications of deep learning methods in materials science, npj Comput. Mater. 8 (1) (2022), https://doi.org/10.1038/s41524-022-00734-6.

[24] J.L. Otto, M. Penyaz, A. Schmiedt-Kalenborn, M. Knyazeva, A. Ivannikov, B. Kalin, F. Walther, Effect of phase formation due to holding time of vacuum brazed AISI 304L/NiCrSiB joints on corrosion fatigue properties, J. Mater. Res. Technol. 9 (5) (2020) 10550–10558, https://doi.org/10.1016/j.jmrt.2020.07.047.

[25] M. Penyaz, J.L. Otto, N. Popov, A. Ivannikov, A. Schmiedt-Kalenborn, F. Walther, B. Kalin, Microstructure influence on corrosion resistance of brazed AISI 304L/NiCrSiB joints, Met. Mater. Int. 27 (2021) 4142–4151, https://doi.org/10.1007/s12540-021-00974-z.

[26] J.L. Otto, M. Penyaz, K. Möhring, L. Gerdes, T. Schaum, A. Ivannikov, A. Schmiedt-Kalenborn, B. Kalin, F. Walther, Microstructure, residual stresses, and strain-rate-dependent deformation and fracture behavior of AISI 304L joints brazed with NiCrSiB filler metals, Metals 11 (4) (2021) 593, https://doi.org/10.3390/met11040593, 1-24.

[27] J.L. Otto, M. Penyaz, A. Schmiedt-Kalenborn, A. Ivannikov, B. Kalin, F. Walther, Influence of alloying and holding time on microstructure and corrosion fatigue behaviour of brazed AISI 304L/NiCrSiB joints. 4, Symposium Materialtechnik (2021) 1–10, https://doi.org/10.21268/20210519-3.

[28] L. Chang, M. Grace Burke, K. Mukahiwa, J. Duff, Y.L. Wang, F. Scenini, The effect of martensite on stress corrosion crack initiation of austenitic stainless steels in high-temperature hydrogenated water, Corros. Sci. 189 (2021), 109600, https://doi.org/10.1016/j.corsci.2021.109600.

[29] I. Park, E.-Y. Kim, W.-J. Yang, Microstructural Investigation of Stress Corrosion Cracking in Cold-Formed AISI 304 Reactor, Metals 11 (7) (2021), https://doi.org/10.3390/met11010007.

[30] X. Chen, M. Gussev, M. Balonis, M. Bauchy, G. Sant, Emergence of micro-galvanic corrosion in plastically deformed austenitic stainless steels, Mater. Des. 203 (2021), 109614, https://doi.org/10.1016/j.matdes.2021.109614.

[31] J. Qian, C. Chen, H. Yu, F. Liu, H. Yang, Z. Zhang, The influence and the mechanism of the precipitate/austenite interfacial C-enrichment on the intergranular corrosion sensitivity in 310 S stainless steel, Corros. Sci. 111 (2016) 352–361, https://doi.org/10.1016/j.corsci.2016.05.021.

[32] L. Yuan, J. Xiong, Y. Du, J. Ren, J. Shi, J. Li, Microstructure and mechanical properties in the TLP joint of FeCoNiTiAl and Inconel 718 alloys using BNi2 filler, J. Mater. Sci. Technol. 61 (2021) 176–185, https://doi.org/10.1016/j.jmst.2020.05.050.

[33] J.K. Kim, H.J. Park, D.N. Shim, D.J. Kim, Effect of bonding parameters on microstructural characteristics during TLP bonding of directionally solidified Ni-based superalloy, J. Manufact. Process. 30 (2017) 208–216, https://doi.org/10.1016/j.jmapro.2017.09.024.

[34] M. Yang, T. Zhang, R. Ding, Z. Qiao, C. Liu, Y. Liu, Microstructure Evolution of Athermal Solidification Zone and Its Effect on Mechanical Properties in Dissimilar Transient Liquid Phase Bonded Joint of IN718 Ni-Based Alloy/316LN Steel, J. Mater. Eng. Perform. (2023) 1–17, https://doi.org/10.1007/s11665-023-07997-0.

[35] M. Pouranvarin, A. Ekrami, A.H. Kokabi, TLP bonding of cast IN718 nickel based superalloy: Process–microstructure–strength characteristics, Mater. Sci. Eng. A 568 (2013) 76–82, https://doi.org/10.1016/j.msea.2013.01.029.